Influence of Austempering Conditions on Hardness and Microstructure of Bainite in Low-Alloyed Steel

ADAM STÅHLKRANTZ, PETER HEDSTRÖM, NIKLAS SARIUS, and ANNIKA BORGENSTAM

The influence of austempering temperature and time on the microstructure and hardness of a low-alloyed bainitic steel is investigated in the temperature range 275 °C to 375 °C for up to 24 hours. It is shown that the dislocation density and coarseness of the bainitic microstructure are affected by the austempering temperature, while only the dislocation density is significantly affected by the austempering time. The hardness of the steel is estimated based on microstructure–property relations and is in good agreement with the measured hardness. In conclusion, the decrease in dislocation density is the main reason for loss in hardness upon increasing austempering temperature and/or time for the studied temperature range.

I. INTRODUCTION

THE continuous improvement of processing of steels, such as more controlled austempering conditions, has provided the industry with more repeatable and precise processes allowing for a more exact tuning of the steel properties and the final performance. This in turn has increased the importance to fully understand how a change in the process affects the microstructure, and thus, the properties to take full advantage of the increased precision in the processing.

To understand how the microstructure and the mechanical properties are affected by different austempering conditions such as time and temperature, experimental data can be used to estimate the strength or hardness from the different microstructural parameters such as grain size, dislocation density, precipitation, and alloying elements in solid solution. However, reality is often much more complex, and some of the parameters are hard to differentiate from each other. Therefore, several assumptions and simplifications must be made. An improved understanding of the material is required to ensure that the right structure–property relations are considered, and that the assumptions and simplifications that are made are reasonable. The understanding of the decisive structure-property relations will also determine the extent of experimental input required to be able to predict properties based on processing conditions and microstructure.

Studies on austempering and tempering of bainite have been performed extensively on high silicon bainitic steels, which due to the high silicon content, have large amounts of retained austenite.[1–8] Low-alloyed steels, on the other hand, do not have significant amounts of retained austenite and bainite-tempering studies on low-alloyed bainitic steels are scarce in the literature. It has been shown in a previous work by the authors[9] that the hardness of bainite is not only dependent on the austempering temperature, but also on the austempering time. However, only one austempering temperature was investigated in that study. Therefore, the same material will here be investigated in a wider austempering temperature range of 275 °C to 375 °C to understand how temperature and time affect the strength and hardness of bainite. The underlying microstructural reasons for the change in hardness and strength are the key considerations in this work. Hence, detailed microstructural characterization is performed, and the results are evaluated using structure–property relations from the literature to study the different microstructural contributions to the hardness evolution during austempering and tempering of bainite. The new understanding of the relation between austempering temperature and time and the mechanical properties (hardness) can help further optimize processing of similar low-alloyed bainitic steels.

ADAM STÅHLKRANTZ, PETER HEDSTRÖM, and ANNIKA BORGENSTAM are with the Department of Material Science and Engineering, KTH Royal Institute of Technology, 114 28 Stockholm, Sweden. Contact e-mail: Adamsta@kth.se NIKLAS SARIUS is with the Husqvarna Group, 561 82 Huskvarna, Sweden.

II. EXPERIMENTAL METHODS

The steel used in this study was a soft-annealed 1.1-mm-thick plate with the chemical composition given in Table I. Samples of size $6 \times 6 \times 1.1$ mm^3 were cut and used for microstructure and hardness investigations and samples of size $10 \times 10 \times 1.1$ mm^3 were used for X-ray diffraction (XRD). All samples were austenitized at 880 °C for 20 minutes in a tube furnace under argon atmosphere followed by quenching in a Bi–Sn metal bath to temperatures in the range 275 °C to 375 °C for isothermal heat treatments with holding times between 10 minutes and 24 hours before quenching in brine.

The time required for full transformation was investigated using a Quenching/Deformation Dilatometer L78 RITA. Samples were cut by wire electrical discharge machining into a geometry of $10 \times 4 \times 1.0$ mm^3. Dilatometry was conducted with a heating rate of 5 °C/s to 880 °C and holding for 20 minutes, followed by quenching to the isothermal heat treatment temperatures in the range of 275 °C to 375 °C with a quenching rate of about 200 to 300 °C/s which was sufficient to avoid any unwanted transformations.

Hardness measurements were performed on hot-mounted samples using a semi-automatic micro-hardness tester Future-Tech FM. Fifteen indents with the load of 1 kg were performed on each sample. All samples were mechanically polished with a finishing step of 1 μm prior to hardness testing.

For microstructural characterization, samples were first mechanically polished in steps with diamond suspension followed by a final polishing step using colloidal silica with a particle size of 0.02 μm. For structural characterization in SEM, backscattered electrons (BSE) and electron backscatter diffraction (EBSD) were used. SEM BSE investigations were conducted in a JEOL JSM-7800F operating at 12 kV with a working distance of 7 mm. For EBSD, a step size of 50 nm was used, and the SEM was operated at 12 kV with a working distance of 20 mm. The post-processing of data was conducted using the software Bruker QUANTAX CrystAlign.

Thickness measurements of bainitic plates were performed from BSE images using a mean linear intercept method.[9] The measurements were stereologically corrected on randomly selected sections of the packets and plates to estimate the true thickness as follows:

$$\overline{L}_T = \frac{\pi}{2} t, \qquad [1]$$

where $\overline{L}_T$ is the measured thickness and t is the true thickness.[10] The packet size was measured using EBSD and QUANTAX CrystAlign.

The size of the cementite was determined from carbon extraction replicas. These were prepared from mechanically polished samples etched with 2 pct picric acid and sputtered with a 100 to 200-Å-thick carbon layer on the surface. The carbon film was cut in 1×1 mm^2 squares and submerged into 7 pct perchloric acid in order to extract the film from the surface. The films were cleaned two times in ethanol followed by distilled water after which they were placed on a Cu grid. The samples were

Table I. The Alloy Composition (Wt Pct)

C	Si	Mn	Cr	Ni	Fe
0.61	0.21	0.36	0.10	0.90	bal.

analyzed in a JEOL JEM-2100F transmission electron microscope (TEM) in scanning mode (STEM) operated at 200 kV.

Samples for XRD investigations were mechanically polished to the final polishing step of 1 μm, followed by electro-polishing in 7 vol pct perchloric acid at 6 V for approximately 30 seconds to remove any mechanically induced strain. The XRD measurements were conducted using a Bruker D8 Discover with Cu-K$_\alpha$ radiation and a LynxEye 1D energy-dispersive detector. The data were recorded from 40 to 141 de 2θ with angular intervals of 0.02 to 0.03 deg and a counting time per step of 5 to 8 seconds. The Cu-K$_{\alpha 2}$ was subtracted from the data using the software DIFFRAC.EVA V4.0, before analyzing the peaks using the software LIPRAS.[11] The peaks were least square fitted using a pseudo-Voigt function. Instrumental peak broadening was determined using an Al$_2$O$_3$ reference sample and was subtracted from the measured peak widths using the closest reference peak with regards to 2θ. The amount of dislocations was calculated from the full width at half-maximum (FWHM) using the Williamson–Hall method,[12,13] which have been described in earlier work.[9]

In addition to the experimental results, complementary thermodynamic calculations were performed to evaluate equilibrium conditions using the Thermo-Calc software and the TCFE9 database.[14,15] The DICTRA software and the TCFE9 and MOBFE4 database were used to estimate the coarsening during austempering, assuming a spherical geometry of the particles, and a ferritic matrix surrounding it. The particle size was set to a radius of 15 nm, which is about the size of the smallest particles observed experimentally, the surface energy was set to 0.7 which can be considered in the higher range,[16,17] this to estimate the highest possible coarsening rate.

III. EXPERIMENTAL RESULTS

A. Transformation and Hardness

To ensure a fully bainitic microstructure after isothermal heat treatment, dilatometry testing was conducted prior to the metal bath heat treatments. The samples were kept at the isothermal temperature until the transformation ceased. The transformation time increased with decreasing austempering temperature, and the longest time required to reach a fully bainitic microstructure was 1052 seconds at 275 °C, Figure 1. To estimate the degree of transformation, 100 pct transformation was assumed to have been reached when the elongation reached 99 pct of the difference between the lowest and highest elongation measured with dilatometry, after quenching to the isothermal temperature. It
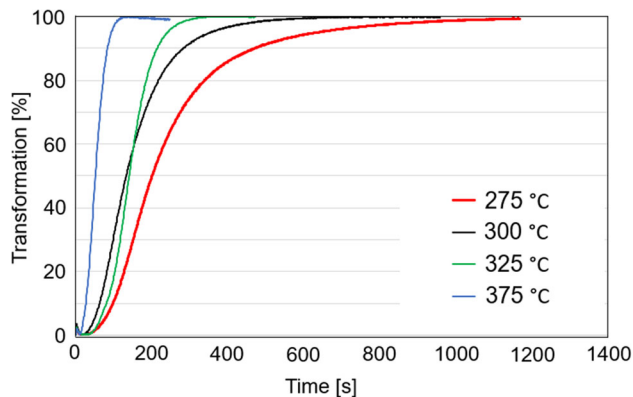
Fig. 1—Degree of transformation of bainitic ferrite for austempering temperatures between 275 °C and 375 °C, calculated from dilatometry data.
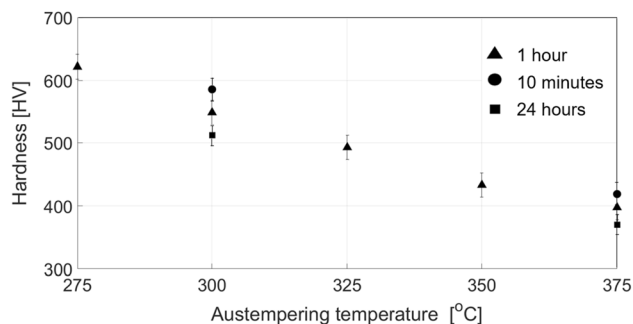

Fig. 2—Hardness as function of austempering temperature after austempering for 1 h between 275 °C and 375 °C and for 10 min and 24 h at 300 °C and 375 °C.

was also confirmed that all austempering temperatures were above the martensite start temperature which was determined by dilatometry to be at about 258 °C.

The hardness decrease with increasing austempering temperature is shown in Figure 2 for an austempering time of 1 hours. The hardness after austempering for, 10 minutes and 24 hours, at 300[9] and 375 °C is also included. It can be seen that the hardness decreases with both increasing austempering temperature and increasing austempering time.

B. *The Bainitic Microstructure*

Bainite is a hierarchical structure consisting of packets and plates where several parallel plates constitute a packet, see Figure 3. The bainitic plates can partly be identified in Figures 3(b) and (c) by the vague lines separating them and occasionally by a difference in contrast when the difference in crystallography is large enough as it is between packets. It can be seen that an increased austempering temperature increases the coarseness of the microstructure, which is evident comparing a, b, and c in Figure 3. This has been shown in more detail in previous works on the same material.[9,18]

However, no visual change in the microstructure can be seen when comparing the microstructures formed after 10 minutes and 24 hours at 375 °C, Figures 3(b)

and (c). The change in microstructure, due to extended austempering time, should have been most profound at the highest temperature, 375 °C, and thus, it can be concluded that the same holds for the lower temperatures. To confirm these observations, a structural analysis is presented in the following sections where different microstructural parameters such as grain size, dislocation density, and size of precipitates are studied in more detail.

C. *Packet and Plate Size*

To determine the plate thickness, a large number of images were analyzed using the same methodology as in previous work[9] to provide an accurate estimation, and the results are given in Table II. It is shown that the austempering temperature influences the plate size while the austempering time did not have any measurable effect. The packet size can be easily observed from EBSD micrographs using inverse pole figure (IPF) coloring, Figures 4(a) through (c), since the packets are separated by high-angle boundaries and colored differently.[9,18] The mean-free path which corresponds to the size of the packets was measured after 1 hour of austempering from the Euler data for all temperatures studied, see Figure 5(a). Different misorientation angle criteria with a threshold varying from 2 to 20 deg were applied. As expected, a higher austempering temperature resulted in a coarser microstructure. It is also shown that by increasing the threshold value of the misorientation angle, the packet size is increased. In Figure 5(b) the effect of austempering time is shown for 10 minutes, 1 and 24 hours, for 300 °C and 375 °C. It is shown that the austempering time has no measurable effect. Further, some retained austenite is observed in the packet boundaries, Figures 4(d) through (f). The presence of retained austenite in the high-angle boundaries has previously been observed,[9] where it also was shown that there is no retained austenite between the bainitic ferrite plates inside the packets.[9]

D. *Cementite Particle Size*

The size of the cementite is known to increase with increasing austempering temperature and was evaluated with TEM operating in STEM mode on carbon replicas after heat treatment for 10 minutes and 24 hours at 300 °C and 375 °C, Table III and Figure 6. An increase of the average size of the cementite with increasing temperature is observed, but no difference is observed between 10 minutes and 24 hours at the same austempering temperature. This is in agreement with DICTRA simulations which show that the coarsening of cementite is negligible after 24 hours at 375 °C. DICTRA furthermore shows that the temperature needs to be increased to about 500 °C before significant coarsening of cementite occurs, see Figure 7. The simulations from 300 °C (yellow dashed line) and 400 °C (blue solid line) overlap, and it is shown that no change in cementite size was observed at these temperatures.
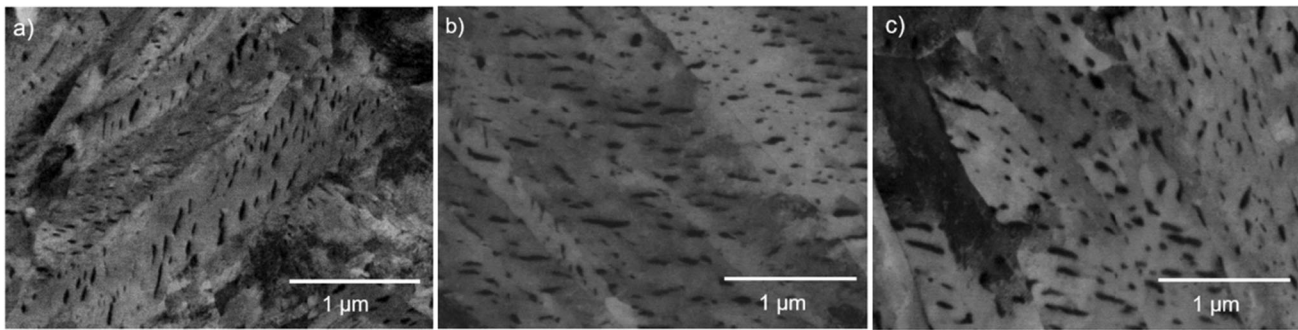
Fig. 3—BSE images after (*a*) 10 min 300 °C, (*b*) 10 min at 375 °C, and (*c*) 24 h at 375 °C. The cementite appears black as they reflect the electrons poorly, some bulkier darker areas are also visible due to electron channeling effects in the bainitic ferrite.

Table II. Plate Thickness After 10 min and 24 h at 300 °C and 375 °C, Error Margins ($\pm$) are the Calculated Standard Error of the Mean

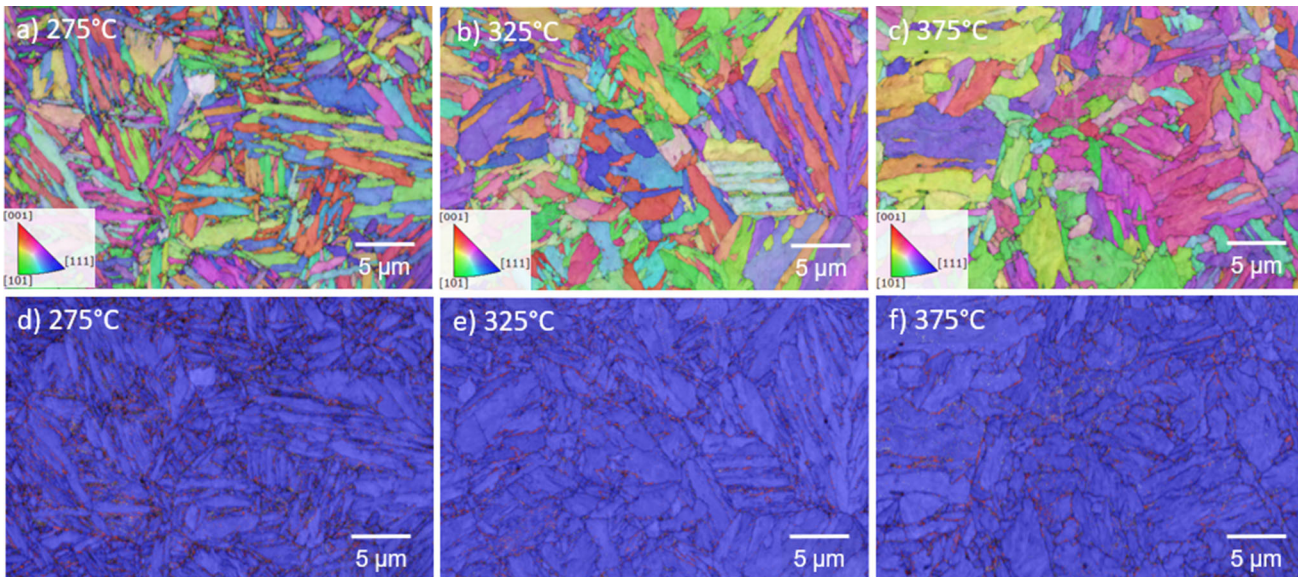| Sample	Number of Plates Measured	Total Number of Images	Measured Thickness (nm)	True Thickness, *t*, from Eq. [1]
300 °C 10 min	321	48	103.6 $\pm$ 1.8	66.0
300 °C 24 h	355	40	100.7 $\pm$ 1.3	64.1
375 °C 10 min	311	40	129.3 $\pm$ 1.8	82.3
375 °C 24 h	281	40	133.8 $\pm$ 1.8	85.2

Fig. 4—(*a* to *c*) EBSD micrographs using pole figure (IPF) coloring for 275 °C, 325 °C, and 375 °C. (*d* to *f*) show the corresponding area with phase mapping, where ferrite is given in blue and austenite in red (Color figure online).

E. *Composition of Bainitic Ferrite*

The carbon content in the bainitic ferrite may be estimated by evaluating the d-spacing of the (222) peak in the same way as in previous work.[9,19] It should be emphasized that since only one sample was evaluated for each temperature and there is a large error related to the estimation from experimental XRD data, it should only be considered as a rough estimate. However, no differences could be determined between the samples from the peak positions in the XRD patterns. Thus, the carbon content appears to be fairly stable over the investigated temperature range. The carbon content is also overlapping with that observed in the soft-annealed reference sample. Therefore, the amount of carbon in the matrix is assumed to be equal to that of the soft-annealed reference sample. The carbon in the reference sample was further assumed to be the equilibrium carbon content in ferrite at the A1 temperature,
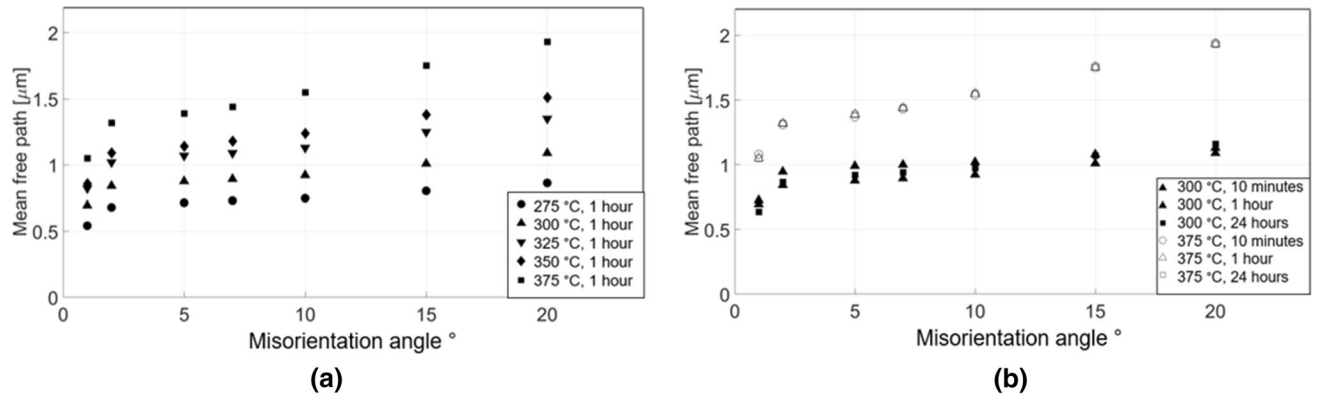
Fig. 5—Mean-free path between packets as function of misorientation angle (*a*) for austempering temperatures 275 °C to 375 °C and (*b*) for austempering temperatures 300 °C and 375 °C for three different times, 10 min, 1, and 24 h.

Table III. Measurements of the Size of Cementite Particles from Carbon Replica with Standard Error of the Mean

Sample	Number	Length (nm)	Width (nm)	Diameter (nm)
10 min 300 °C	298	91 ± 2.7	38.6 ± 0.8	65
24 h 300 °C	277	85 ± 2.0	40.3 ± 1.0	63
10 min 375 °C	296	125 ± 3.0	56 ± 1.0	91
24 h 375 °C	287	126 ± 3.4	55 ± 1.2	91

The diameter is calculated as an average of the length and the width.

which is close to soft annealing temperature, and was calculated to be 0.019 wt pct using the Thermo-Calc software.[14]

Bainitic ferrite is formed under para equilibrium conditions, and the content of substitutional alloying elements will, according to DICTRA simulations, not change during austempering at the investigated times and temperatures. Therefore, the content of substitutional alloying elements can be taken from the nominal composition in Table I. However, it should be mentioned that after tempering for 1 hours above 400 °C it has been shown that it may be of importance to consider diffusion especially at interfaces.[6,20–23]

F. Dislocation Density

The dislocation density in the material was measured after austempering for 1 hours in the temperature range 275 °C to 375 °C and, after 10 minutes and 24 hours at 300 °C and 375 °C. The dislocations density was calculated from the XRD data by analyzing the changes in the peak broadening for the ferritic peaks using the FWHM, and then applying the Williamson–Hall method.[12,13] It can be seen that the dislocation density is highly dependent on austempering temperature, Figure 8, but also on austempering time.

IV. ESTIMATION OF HARDNESS

The strength of a material consists of different parts such as grain boundary strengthening, σ_{GB}, precipitation strengthening, σ_p, solid solution strengthening, σ_{ss}, Peierls–Nabarro friction, σ_{PN}, and dislocation strengthening, σ_d, and can be summed as follows:

$$\sigma_{tot} = \sigma_{GB} + \sigma_p + \sigma_{ss} + \sigma_{PN} + \sigma_d. \quad [2]$$

By estimating the different contributions based on experimental results, the total hardness can be calculated and compared to the measured hardness. The standard DIN 50150 was used to convert the calculated strength into a hardness value. It should be noted that several of the individual contributions from the microstructure is hard to decipher individually as they are interlinked, but the equations do provide an approximation for the magnitude of the contribution from each strengthening mechanism to the total strength.

A. Grain Boundary Strengthening

In bainitic structures there are both high and low angle boundaries that could pose an obstacle to dislocation movement and, thus, increase the hardness. Bainitic plates are only separated with a minimal misorientation boundary which only pose a small obstacle for dislocation movement[24–27] and has, thus, a very small hardness contribution unless there is retained austenite between the plates which would act as a significant obstacle for dislocation movement. In the current material, no retained austenite has been observed in the plate boundaries in contrast to high silicon bainitic steels where plate boundaries have a major contribution to the strength, due to the retained austenite in-between the plates.[5,28–30] It has been
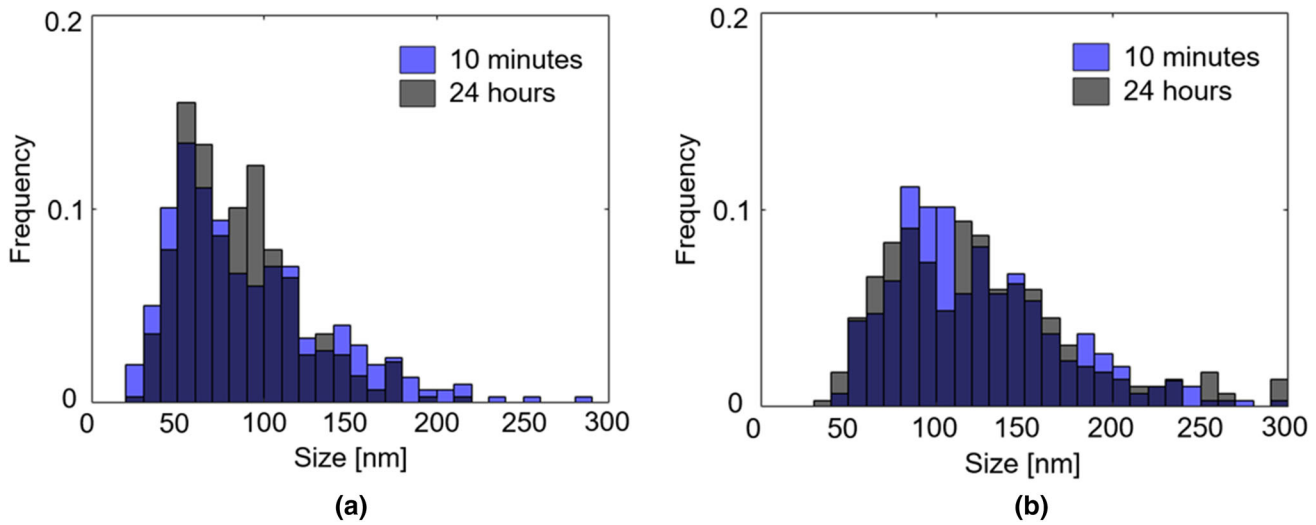
(a)

(b)

Fig. 6—The size distribution for the measured length of the cementite particles after 10 min (blue) and 24 h (gray) at (*a*) 300 °C and (*b*) 375 °C (Color figure online).
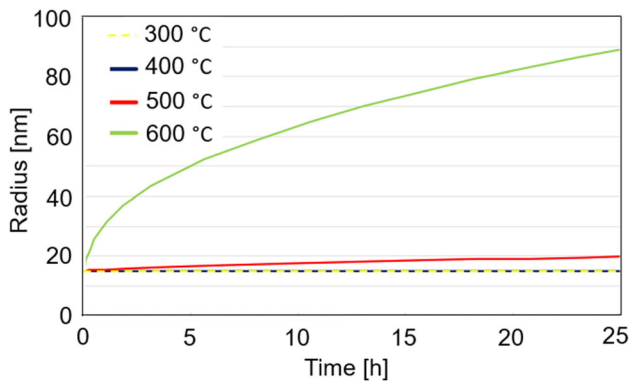

Fig. 7—The cementite particle size calculated with DICTRA simulations for tempering at 300 °C to 600 °C for up to 25 h.
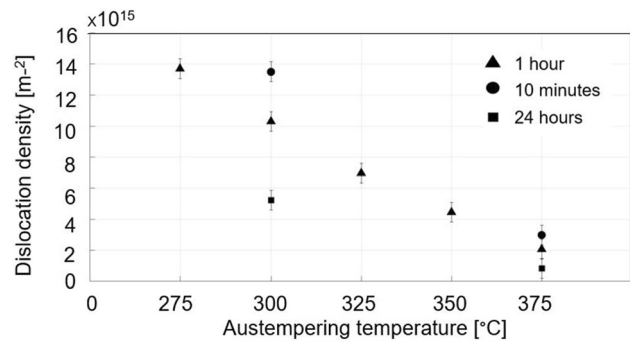

Fig. 8—Measured dislocation density after 1 h in the temperature range 275 °C to 375 °C and after 10 min and 24 h at 300 °C and 375 °C.

argued though that the boundaries between the plates do have an influence even if there is no retained austenite.[24,31] However, the misorientation between the bainite plates herein is very low since the plates grow in parallel and merge forming a packet.[18,32,33] Thus, the plates inside one packet will have the same crystallographic direction, and this is also the reason to why plate boundaries cannot be distinguished in the EBSD images.[18,34] The high-angle boundaries found between the packets will, however, pose a much larger obstacle and is, therefore, assumed to be the major contributor for the grain boundary strengthening in this material. This is supported by similar studies in martensite where Morito *et al.* concluded that the high-angle boundaries are the major contributors.[35]

To calculate the grain boundary strengthening, the Hall–Petch[36,37] relation was used:

$$\sigma_{GB} = K_{HP} * d^{-\frac{1}{2}} \qquad [3]$$

where K_{HP} is a constant, herein set to 500 MPa $\mu m^{1/2}$, and d is the size in μm, which is here taken as the packet size, evaluated in Figure 5(a). The misorientation angle

criterion chosen was 15 deg to represent the packet boundaries.[38] The calculated Hall–Petch contribution to the hardness is linearly dependent of the austempering temperature and presented together with the other strengthening contributions in Figure 9. It should be mentioned that the value of K_{HP} varies in the literature and is dependent on the choice of barriers and is usually in the range of 100 to 800 MPa $\mu m^{1/2}$.[8,27,35,39] It can be noted that where only packet boundaries are used, a larger K_{HP} value is generally chosen compared to when plate boundaries are used to define the barriers.

B. Precipitation Strengthening

The contribution to the strength from the cementite particles is calculated using the Orowan stress[40]

$$\sigma_p \hat{=} \alpha G b \frac{\sqrt{f}}{r}, \qquad [4]$$

where *f* is the volume fraction of cementite, r the particle radius, G the shear modulus, *b* the Burgers vector, and α is a numerical constant, herein set to 1.66.[41,42] The
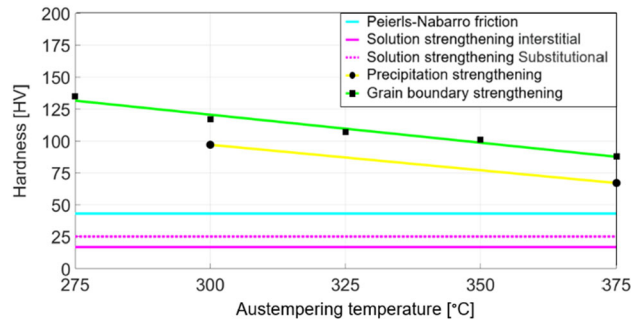
Fig. 9—The individual hardness contributions form Peierls–Nabarro friction, solid solution strengthening, grain boundary strengthening, and precipitation strengthening as function of austempering temperature. The calculated hardness contribution for grain boundary (black squares) and precipitation strengthening (black circles) is also included.

Table IV. Strengthening Coefficients for Solid Solution Strengthening

Element	C	Si	Ni	Mn	Cr
β_i MPa (wt pct)	3700	108	40	48	9

amount of cementite in the material is assumed to be equal to the equilibrium amount at 300 °C calculated using Thermo-Calc, 9.3 Vol pct. Since the size was shown to be the same regardless of the austempering time, an average size was calculated from the data in Table III. The hardness contribution from the cementite particle after austempering at 300 °C and 375 °C is given in Figure 9. It is further assumed that the size of the cementite will increase linearly with increasing austempering temperature. Thus, a line was drawn between the two calculated values based on the measured size of the cementite at 300 °C and 375°C giving an approximation of the temperature dependence.

C. Solid Solution Strengthening

The contribution of solid solution strengthening was calculated as follows:

$$\sigma_{ss} = \sum_i (\beta_i X_i), \qquad [5]$$

where X_i is the composition in weight pct and the β_i coefficients are given in Table IV.[43,44] The contribution from the substitutional elements (Si, Ni, Mn, Cr), using the compositions in Table I as previously described, gives a contribution of 25 HV. To estimate the contribution to solid solution strengthening from carbon, the content previously estimated to 0.019 wt pct was used, and the contribution was determined to 17 HV. It can be mentioned that the contribution from carbon could be higher if other equations and coefficients were to be used[45,46] indicating the uncertainty and complexity for the determination of the contribution to the strength from carbon.
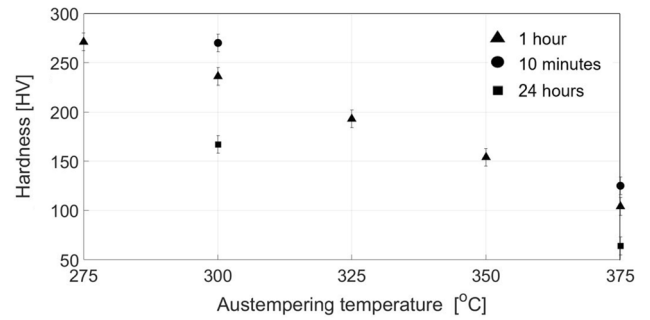

Fig. 10—The hardness contribution from dislocations for the temperature range 275 °C to 375 °C after 1 h of austempering with two additional times 10 min and 24 h for 300 °C and 375 °C included.

Further, the effect of solid solution strengthening of carbon is challenging to differentiate from the contribution from dislocation strengthening since they probably are related through Cottrell atmospheres. The close connection between dislocations and carbon have been shown earlier in a detailed study of the same material for extended isothermal heat treatment.[9] It could, further, be speculated that during annihilation of dislocations, the carbon atoms in the Cottrell atmospheres connected to the specific dislocation would diffuse to a nearby cementite particle or to the carbon-enriched austenite films in the packet boundaries. Cementite could also nucleate which could give an increase in hardness. According to the DICTRA simulations, carbon should be able to move freely in the ferrite at the investigated temperature range. The carbon atoms could also cling to dislocations in other Cottrell atmospheres and create larger clusters of carbon around the remaining dislocations.

D. Peierls–Nabarro Friction

The friction in the lattice of the material hindering the dislocation movement is often referred to as Peierls–Nabarro friction,[47,48] which describes the energy required for a dislocation to move. This results in a temperature and time dependence, where the dislocations can move when the activation energy to surpass the Peierls–Nabarro friction is overcome.[49–51] For pure iron, the hardness contribution was set to 43 HV[39] and was assumed to be constant over the investigated temperature range herein. The contribution is included in Figure 9.

E. Dislocation Strengthening

The contribution from dislocations to the strength can be calculated using

$$\sigma_d = \approx 7.34 \rho_d^{\frac{1}{2}}, \qquad [6]$$

where ρ_d is the dislocation density.[52] The hardness contribution from the experimentally determined dislocation density for different austempering temperatures and times is presented in Figure 10 based on the
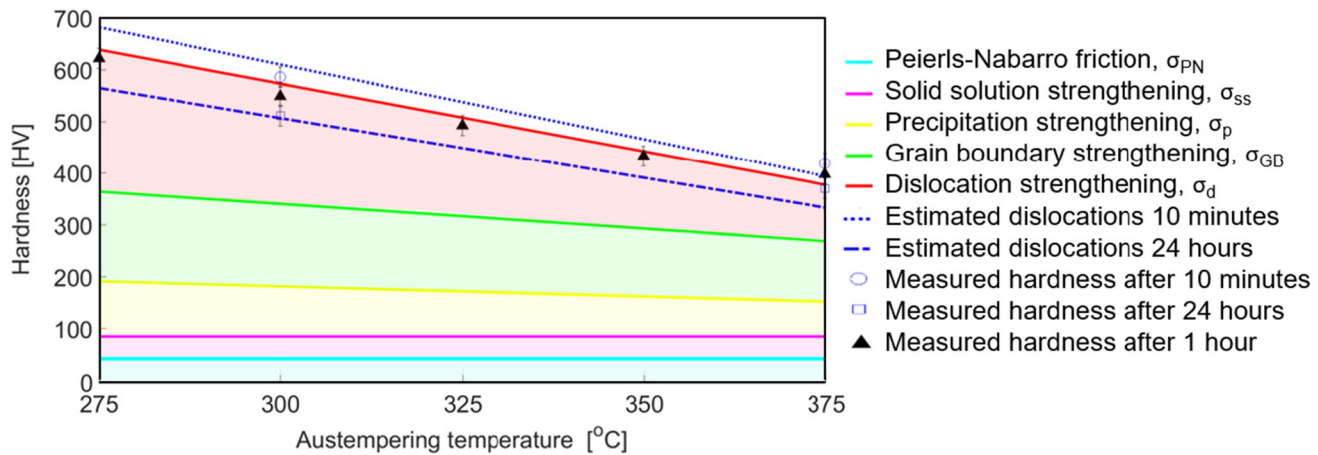
Fig. 11—The individual estimated hardness contributions stacked together, the total contribution from each is colored under its line in the same color as the line. The contribution from the dislocations after 1 h is presented as the red shaded area, further, the dislocation contribution estimated after 10 min and 24 h is indicated with the blue-dotted and dash-dotted lines, respectively. The experimentally measured hardness after 1 h is indicated with the black triangles, while the experimentally measured hardness after 10 min and 24 h at 300 °C and 375 °C is indicated with hollow circles and squares, respectively (Color figure online).

dislocation densities presented in Figure 6. The decrease in dislocation density with increasing temperature can be explained by less hindrance at the dislocation movement due to lower amount of grain boundaries, and larger cementite particles. The higher austempering temperature also provides a higher energy available for the dislocation movement resulting in higher recovery rate during and after the transformation. Further the hardness after 10 minutes and 24 hours is also assumed to vary linearly with temperature as for the 1 hours austempered samples, and it is also assumed that it can be extrapolated to 275 °C.

F. Total Hardness

The total hardness can be estimated by summing the individual contributions presented in Figures 9 and 10. The variation of total hardness with temperature and time is presented in Figure 11. The experimentally measured hardness is also included in Figure 11, and it is shown that the estimated hardness is in good agreement with the measured hardness. It can be noted that the increase in coarseness of the microstructure with increasing austempering temperature has a rather small impact on the decrease in hardness, and the most significant effect comes from the decrease in dislocation density. The influence of austempering time was calculated for 300 °C and 375 °C and is assumed to follow a linear trend presented as dotted and dash-dotted lines, which indicated the change in hardness between 10 minutes and 24 hours austempering.

calculated hardness based on microstructural data and experimentally measured hardness is very good. This agreement could be seen for the change of hardness with respect to both austempering temperature and austempering time. It was further shown that packet, plate, and cementite size are defined by the austempering temperature but did not change significantly with austempering time for the investigated temperature range of 275 °C to 375 °C. On the other hand, the dislocation density was strongly affected by both austempering time and temperature. It is concluded that the decrease in dislocation density is the main reason for the hardness decrease with increasing austempering temperature and time for bainite in low-alloyed steel.

V. CONCLUSIONS

It has been shown how different microstructural features may contribute to the total hardness of bainite in a low-alloyed bainitic steel. The agreement between

CONFLICT OF INTEREST

On behalf of all authors, the corresponding author states that there is no conflict of interest.

REFERENCES

1. C. Garcia-Mateo, M. Peet, F. Caballero, and H. Bhadeshia: *Mater. Sci. Technol.*, 2004, vol. 20, pp. 814–18.
2. C. Garcia-Mateo and F. Caballero: *ISIJ Int.*, 2005, vol. 45, pp. 1736–40.
3. M. J. Peet, University of Cambridge, Cambridge, UK, 2010.
4. A. S. Podder, University of Cambridge, Cambridge, UK, 2011.
5. M.J. Peet, S.S. Babu, M.K. Miller, and H. Bhadeshia: *Metall. Mater. Trans. A*, 2017, vol. 48A, pp. 3410–18.
6. F.G. Caballero, M.K. Miller, C. Garcia-Mateo, C. Capdevila, and S.S. Babu: *Acta Mater.*, 2008, vol. 56, pp. 188–99.
7. F.G. Caballero, M.K. Miller, A. Clarke, and C. Garcia-Mateo: *Scr. Mater.*, 2010, vol. 63, pp. 442–45.
8. S. He, B. He, K. Zhu, and M. Huang: *Acta Mater.*, 2017, vol. 135, pp. 382–89.
9. A. Ståhlkratnz, P. Hedström, N. Sarius, H.-Å. Sundberg, S. Kahl, M. Thuvander, and A. Borgenstam: *Metall. Mater. Trans. A*, 2020, vol. 51A, pp. 6470–81.
10. L. Chang and H. Bhadeshia: *Mater. Sci. Technol.*, 1995, vol. 11, pp. 874–82.
11. G. Esteves, K. Ramos, C.M. Fancher and J.L. Jones: Preprint at https://www.researchgate.net/publication/316985889_LIPRAS_Line-Profile_Analysis_Software, 2017.
12. G. Williamson and R. Smallman: *Philos. Mag.*, 1956, vol. 1, pp. 34–46.
13. G. Williamson and W. Hall: *Acta Metall.*, 1953, vol. 1, pp. 22–31.
14. J.-O. Andersson, T. Helander, L. Höglund, P. Shi, and B. Sundman: *Calphad*, 2002, vol. 26, pp. 273–312.
15. A. Borgenstam, L. Höglund, J. Ågren, and A. Engström: *J. Phase Equilib.*, 2000, vol. 21, p. 269.
16. Z. Hou, P. Hedström, Q. Chen, Y. Xu, D. Wu, and J. Odqvist: *Calphad*, 2016, vol. 53, pp. 39–48.
17. X. Xiao, G. Liu, B. Hu, J. Wang, and W. Ma: *J. Mater. Sci.*, 2013, vol. 48, pp. 5410–19.
18. A. Ståhlkrantz, P. Hedström, N. Sarius, and A. Borgenstam: *Metall. Mater. Trans. A*, 2021, vol. 52A, pp. 4546–57.
19. D. Dyson: *J. Iron Steel Inst.*, 1970, vol. 208, pp. 469–74.
20. G. Miyamoto, J. Oh, K. Hono, T. Furuhara, and T. Maki: *Acta Mater.*, 2007, vol. 55, pp. 5027–38.
21. W. Song, P.-P. Choi, G. Inden, U. Prahl, D. Raabe, and W. Bleck: *Metall. Mater. Trans. A*, 2014, vol. 45A, pp. 595–606.
22. C. Zhu, X. Xiong, A. Cerezo, R. Hardwicke, G. Krauss, and G. Smith: *Ultramicroscopy*, 2007, vol. 107, pp. 808–12.
23. F.G. Caballero, M.K. Miller, S.S. Babu, and C. Garcia-Mateo: *Acta Mater.*, 2007, vol. 55, pp. 381–90.
24. C. Du, J. Hoefnagels, R. Vaes, and M. Geers: *Scr. Mater.*, 2016, vol. 116, pp. 117–21.
25. T. Ohmura, A. Minor, E. Stach, and J. Morris: *J. Mater. Res.*, 2004, vol. 19, pp. 3626–32.
26. A. Shibata, T. Nagoshi, M. Sone, S. Morito, and Y. Higo: *Mater. Sci. Eng. A*, 2010, vol. 527, pp. 7538–44.
27. G. Gao, B. Gao, X. Gui, J. Hu, J. He, Z. Tan, and B. Bai: *Mater. Sci. Eng. A*, 2019, vol. 753, pp. 1–10.
28. F.G. Caballero and H.K.D.H. Bhadeshia: *Curr. Opin. Solid State Mater. Sci.*, 2005, vol. 8, pp. 251–57.
29. A.S. Podder, I. Lonardelli, A. Molinari, and H. Bhadeshia: *Proc. R. Soc. A*, 2011, vol. 467, pp. 3141–56.
30. A.S. Podder and H.K.D.H. Bhadeshia: *Mater. Sci. Eng. A*, 2010, vol. 527, pp. 2121–28.
31. K. Zhu, O. Bouaziz, C. Oberbillig, and M. Huang: *Mater. Sci. Eng. A*, 2010, vol. 527, pp. 6614–19.
32. J. Yin, M. Hillert, and A. Borgenstam: *Metall. Mater. Trans. A*, 2017, vol. 48A, pp. 1425–43.
33. J. Yin, M. Hillert, and A. Borgenstam: *Metall. Mater. Trans. A*, 2017, vol. 48A, pp. 1444–58.
34. A. Ståhlkrantz, P. Hedström, N. Sarius, and A. Borgenstam: *Metall. Mater. Trans. A*, 2022, vol. 53A, pp. 3418–27.
35. S. Morito, H. Yoshida, T. Maki, and X. Huang: *Mater. Sci. Eng. A*, 2006, vol. 438, pp. 237–40.
36. E. Hall: *Proc. Phys. Soc. Lond. Sect. B*, 1951, vol. 64, p. 747.
37. N.J. Petch: *J. Iron Steel Inst. Lond.*, 1953, vol. 174, pp. 25–28.
38. S. He, B. He, K. Zhu, and M. Huang: *Acta Mater.*, 2018, vol. 149, pp. 46–56.
39. Z.C. Cordero, B.E. Knight, and C.A. Schuh: *Int. Mater. Rev.*, 2016, vol. 61, pp. 495–512.
40. E. Orowan: Institute of Metals, London, 1948, 451–53.
41. W.B. Durham, C. Goetze, and B. Blake: *J. Geophys. Res.*, 1977, vol. 82, pp. 5755–70.
42. S. Takeuchi and A.S. Argon: *J. Mater. Sci.*, 1976, vol. 11, pp. 1542–66.
43. Pickering, F. and T. Gladman, Metallurgical developments in carbon steels. ISI Special Report, 1963, vol. 81.
44. H.K.D.H. Bhadeshia and S.R. Honeycombe: *Steels*, 3rd ed. Butterworth-Heinemann, Oxford, 2016.
45. G.R. Speich and H. Warlimont: *J. Iron Steel Inst.*, 1968, vol. 206, pp. 385–92.
46. P. Winchell. and M. Cohen: 1962, Massachusetts Institute of Technology.
47. R. Peierls: *Proc. Phys. Soc.*, 1940, vol. 52, p. 34.
48. F. Nabarro: *Proc. Phys. Soc.*, 1947, vol. 59, p. 256.
49. A. Evans and R. Rawlings: *Phys. Stat. Sol.*, 1969, vol. 34, pp. 9–31.
50. H. Conrad: *JOM*, 1964, vol. 16, pp. 582–88.
51. G. Schoeck: *Phys. Stat. Sol.*, 1965, vol. 8, pp. 499–507.
52. H.K.D.H. Bhadeshia, *Bainite in Steels: Theory and Practice*, 3rd edn. 2015, Wakefield: Maney Publishing on behalf of the Institute of Materials, Minerals & Mining.